Orientation, Sphericity and Roundness Evaluation of Particles Using Alternative 3D Representations

Irving Cruz-Matías and Dolors Ayala
Department de Llenguatges i Sistemes Informátics,
Universitat Politécnica de Catalunya, Barcelona, Spain

December 2013

Abstract

Sphericity and roundness indices have been used mainly in geology to analyze the shape of particles. In this paper, geometric methods are proposed as an alternative to evaluate the orientation, sphericity and roundness indices of 3D objects. In contrast to previous works based on digital images, which use the voxel model, we represent the particles with the Extreme Vertices Model, a very concise representation for binary volumes. We define the orientation with three mutually orthogonal unit vectors. Then, some sphericity indices based on length measurement of the three representative axes of the particle can be computed. In addition, we propose a ray-casting-like approach to evaluate a 3D roundness index. This method provides roundness measurements that are highly correlated with those provided by the Krumbein's chart and other previous approach. Finally, as an example we apply the presented methods to analyze the sphericity and roundness of a real silica nano dataset.

Contents

Chapter 1

Introduction

In-silicon experimentation is getting a growing interest in bioengineering and geology where scientific data coming from real samples are used to compute structural parameters that allow to evaluate physical properties of a sample such as osteoporosis degree of bones, suitability of biomaterials to be used as implants, grain shape and sphericity index in silica sand for industrial and manufacturing applications, among others.

In geology, the shape description of particles such as grain of sand or rocks have been analyzed since long time to understand different natural processes. Among the most studied parameters of shape description we can mention the pore structure analysis [39, 30] and the orientation, sphericity and roundness, which we study in this paper. The orientation may be defined by rotation angles around a set of orthogonal axes [16]. Preferred orientation arises when the shape is oriented preferentially in a certain directions or set of directions [34] and is related to the anisotropy [26], which refers to the exhibition of different values of a property when measured in different directions. Sphericity is a measure of the degree to which a particle approximates the shape of a sphere, and is independent of its size. Roundness is the measure of the sharpness of a particle's edges and corners. Sphericity and roundness are ratios and, therefore, dimensionless numbers.

Sphericity and roundness are numerically quantified. However, the determination of sphericity and roundness based on Wadell's original definition [41] is difficult. Particle's surface area is necessary to compute the Wadell's sphericity index. This manual measurement is neither easy nor accurate. Therefore, for practical reasons geologists typically use simplified parameters and visual charts [20] with several categories of sphericity and roundness. There are also methods that use 3D devices, but such imaging and interpretation are very time consuming and not suitable for microparticles.

In this paper, we propose alternative geometric methods to evaluate the orientation, sphericity and roundness of 3D objects. Our objective is to reduce the time required to estimate such parameters. The contributions of this paper are:

- A method to define the orientation based on Oriented Bounding Boxes (OBB) that is computed using a previously developed model, the Extreme Vertices Model (EVM) [2, 29].

- An EVM-based method to compute a true 3D roundness index.
- Study of correlation between the developed methods and those reported in the literature.
- A complete analysis of a real silica nano dataset applying the proposed methods and comparing the results with others.

Chapter 2

Related Work

2.1 Orientation

The basic method to describe the orientation of a 3D object is by means of the eigenvectors of the covariance matrix associated to the point set of the object. An oriented bounding box (OBB) [14] is a box which may be arbitrarily oriented (rotated), i.e. its faces are not necessarily aligned with the main coordinate axes. An OBB for a set of points can be created from their eigenvectors.

Preferred orientations are used to predict stiffness and strength in production of fabric tensors [19] or to observe the mass transport phenomena in ionic crystalline materials [33]. In geology, orientation of many clasts in a soil sample can be collected and compared graphically to provide information about their transport history and the characterization of depositional environments [15].

2.2 Sphericity and Roundness

Sphericity and roundness are measures of two different morphological properties. Sphericity is most dependent on elongation, whereas roundness is largely dependent on the sharpness of angular protrusions (convexities) and indentations (concavities) from the object.

Sphericity may be calculated for any 3D object if its surface area and volume are known. Wadell [41] defined the sphericity, Ψ, of an object as the ratio of the nominal surface area (surface area of a sphere having the same volume as the object) to the actual surface area of the object. This ratio is known as true sphericity index:

$$\Psi = \frac{\mathcal{S}_n}{\mathcal{S}} = \frac{(36\pi\mathcal{V}^2)^{\frac{1}{3}}}{\mathcal{S}} \tag{2.1}$$

where $\mathcal{V}$, $\mathcal{S}$ and $\mathcal{S}_n$ are the volume, surface area and nominal surface area of the object respectively. The sphericity index of a sphere is 1 and, by the isoperimetric inequality, any object which is not a sphere will have a sphericity value less than 1.

Since manual measures of $\mathcal{S}$ are very difficult, other indices have been defined. Several methods are based on length measurement of the three representative axes of an object [20]: a (major axis length), b (medium axis length) and

c (minor axis length). The next equations are used frequently in geology:

$$\Psi = \quad d_n/a \tag{2.2}$$

$$\Psi = \quad (bc/a^2)^{\frac{1}{3}} \tag{2.3}$$

$$\Psi = \quad c/(ab)^{\frac{1}{2}} \tag{2.4}$$

$$\Psi = \quad (c^2/ab)^{\frac{1}{3}} \tag{2.5}$$

Eq. 2.2 is a simplified sphericity index proposed by Wadell [42], where d_n is the nominal diameter (diameter of the sphere having the same volume as the object). The index given by Eq. 2.3 is called elliptical volume sphericity [20]. The sphericity index given by Eq. 2.4 provides more precision for the computation of other behavioral indices [6]. A more widely accepted sphericity index is given by Eq. 2.5 as it correlates highly with the particle settling velocity [37].

Concerning roundness, due to the impracticality of measuring a true 3D roundness index, several methods work with the maximum 2D projection plane (silhouette) of the object looking for a trade-off between accuracy and time. Roundness ($\mathcal{R}$) was defined by Wadell [41] as the ratio of the average radius of curvature of the corners and edges of the object's silhouette to the radius of the maximum circle that can be inscribed.

$$\mathcal{R} = \frac{\frac{1}{n}\sum_{i=1}^{n} r_i}{r_{max}} \tag{2.6}$$

where r_i is the radius of the i-th corner curvature, n the number of corners, and r_{max} the radius of the maximum inscribed circle. The value of $\mathcal{R}$ is 1 for a perfectly round object and less than 1 for any other object.

Results of this method are reliable but time consuming and very impractical as no definition of curvature was established [32]. In order to improve the time required to estimate the roundness, Krumbein [20] created a chart (see Fig. 2.1) showing examples of pebbles for which the roundness of their silhouette has been calculated using Eq. 2.6 and grouped them into nine classes.

After Krumbein, other methods provide estimated values that are linearly correlated with the values given by the Krumbein's chart (KC). A method based on the Fourier transform [9] makes use of the sum of the amplitudes of the first 24 coefficients of the Fourier transform. To compensate for different size rocks fragments, the coefficients are divided by the zero-th coefficient and the sphericity aspect is eliminated by This method shows a correlation of 0.94 with the values of KC. An alternative approach uses granulometric methods [10]. The ratio between particle's area before and after applying a morphological opening on its silhouette is a roundness index. This method shows a correlation of 0.96 with the values of KC. Discrete geometry has been used to calculate the Wadell's original index [32]. The curvature radius at each pixel of the silhouette is calculated with an algorithm that relies on the decomposition of a discrete curve into maximal blurred segments [25]. This method shows a correlation of 0.92 with the values of KC.

A true 3D roundness index of gravel shapes was proposed using a laser scanner [17]. The idea is that the ratio between the volume and surface area of an object reflects the roundness. As the ratio $\mathcal{V}/\mathcal{S}$ tends to increase with an increase in size, this ratio is divided by a representative gravel length. Using an ellipsoid

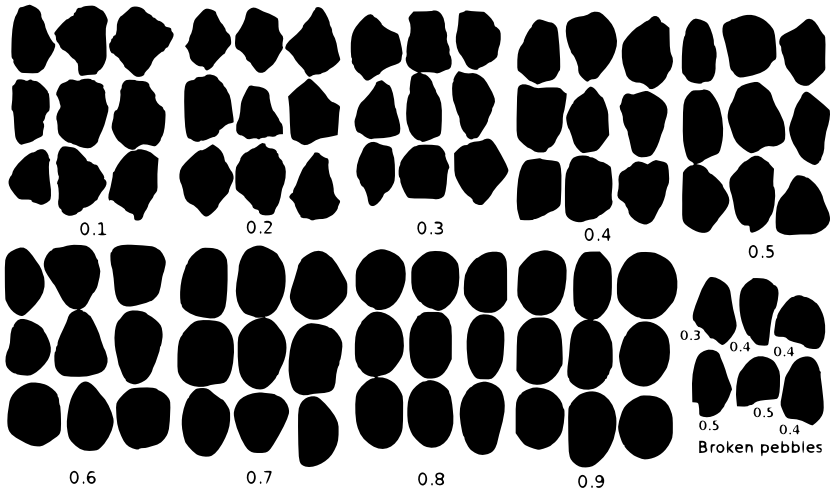

Figure 2.1: Krumbein's chart for visual determination of roundness [20].

as analog of gravel shape, the geometric mean of the three representative axes of the object (a, b, and c) is used as the representative length. The resulting index of the next equation shows a correlation of 0.814 with the values of KC.

$$\mathcal{R} = \frac{\mathcal{V}}{\mathcal{S}(abc)^{\frac{1}{3}}} \tag{2.7}$$

However, the use of a laser scanner to compute the roundness is a very time consuming process for multiple shapes, and not suitable for microparticles.

Chapter 3

Representation Model

The most common model to represent 3D binary digital images is the voxel model, but several proposals represent these images in a more compact way. A binary voxel model represents an object as the union of its foreground voxels and its continuous analog is an orthogonal pseudo-polyhedra (OPP) [18, 21]. In this paper, we represent 3D binary digital images as well as OPP with the Extreme Vertices Model.

OPP have been used in 2D to represent the extracted polygons from numerical control data [27]. Some 3D applications of OPP are: general computer graphics applications such as geometric transformations and Boolean operations [1, 5, 12], connectivity computation [7], virtual porosimetry [30], skeleton computation [11, 22], and orthogonal hull computation [3, 4]. OPP have been also used for model simplification [8].

3.1 Extreme Vertices Model

Let P be an OPP, a *brink* is the maximal uninterrupted segment built out of a sequence of collinear and contiguous two-manifold edges of P and its ending vertices are called *extreme vertices* (EV). An OPP can be represented in a concise way with a sorted set of its EV and such representation scheme is called EVM. EVM is an implicit B-Rep model and therefore represents OPP unambiguously [40].

EVM only needs to store EV, with no additional information such as neighboring relations among vertices, edges, or faces, since all these elements can be computed from them. Therefore, the storage requirements for an OPP P in its EVM representation is $O(n)$, n being the number of EV, and $n \leq v$, where v is the total number of vertices. See Fig. 3.1. For more details concerning EVM see [2] and [29].

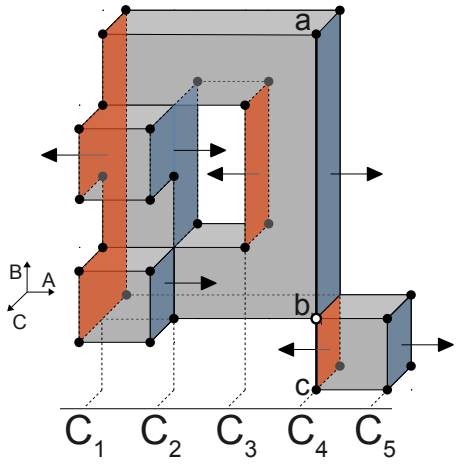

Figure 3.1: An EVM-encoded OPP. Extreme vertices marked with dots; a vertical brink from vertex a to c is marked where these vertices are both extreme vertices while vertex b is not.

Chapter 4

Sphericity and Roundness Evaluation

In this chapter, we present methods to evaluate the orientation, sphericity and roundness of particles represented with EVM. In order to compute the three representative axes of the object, its oriented bounding box (OBB) is obtained first (see Sec. 4.1). Then, several sphericity indices can be computed (see Sec. 2.2).

Additionally, a 3D roundness index is proposed. Sec. 4.3 presents a ray-casting-like approach based on EVM that uses basic geometric methods such as a transformation matrix and the ray-ellipsoid intersection.

4.1 Oriented Bounding Box Computation

An OBB can be represented with a center point $\mathbf{c}$, three edge half-lengths h_1, h_2 and h_3, and an orientation specified with three mutually orthogonal unit vectors $\mathbf{v}^1$, $\mathbf{v}^2$ and $\mathbf{v}^3$ (see Fig. 4.1):

$$OBB = \left\{ \mathbf{c} + \sum_{i=1}^{3} x_i h_i \mathbf{v}^i \ : \ x_i \in [-1, 1] \right\} \tag{4.1}$$

The OBB of an object can be constructed by examining an associated point set. This set forms a cloud and have some statistical distribution characterized by a mean $\mathbf{m} = (m_1, m_2, m_3)$, and a covariance matrix $\mathbf{C}$. The mean describes the center of mass and the covariance matrix contains information about how the cloud is approximately spread out. Eigenvectors of that matrix give the orientation along which the cloud has maximum and minimum statistical spread [13].

The OBB produced with the covariance method may not be a tight fit if the points are not well distributed. However, as the set of points to be evaluated are binary volumes coming from real samples, a good distribution can be expected.

Given a set of n 3D points, viewed as vectors with initial point at the origin: $\mathbf{p}^1, \mathbf{p}^2, \ldots, \mathbf{p}^n$, such that $\mathbf{p}^k = (p_1^k, p_2^k, p_3^k)$, the mean is defined as:

$$m_i = \frac{1}{n} \sum_{k=1}^{n} p_i^k, \quad i = 1, 2, 3 \tag{4.2}$$

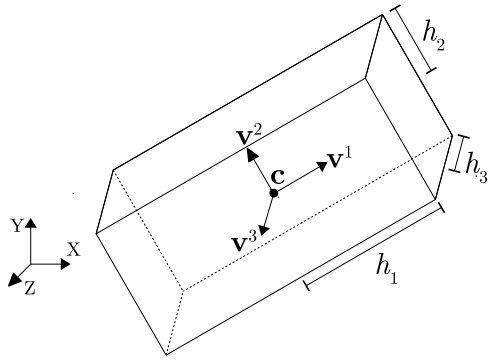

Figure 4.1: A 3D arbitrarily oriented bounding box.

and the 3×3 covariance matrix $\mathbf{C}$ is defined as:

$$\mathbf{C}_{ij} = \left(\frac{1}{n} \sum_{k=1}^{n} p_i^k p_j^k \right) - m_i m_j, \quad i,j = 1,2,3 \tag{4.3}$$

The normalized eigenvectors of matrix $\mathbf{C}$ ($\mathbf{v}^1$, $\mathbf{v}^2$ and $\mathbf{v}^3$) represent the orientation vectors of the OBB. The lower ($L = \{l_1, l_2, l_3\}$) and upper ($U = \{u_1, u_2, u_3\}$) extremes along each axis are given by projecting all points $\mathbf{p}^k$ onto each eigenvector and checking the minimum (m) and maximum (M) coordinates in each direction:

$$L = \left\{ m(\mathbf{v}^1 \cdot \mathbf{p}^k),\ m(\mathbf{v}^2 \cdot \mathbf{p}^k), m(\mathbf{v}^3 \cdot \mathbf{p}^k) \right\}, \quad \forall\ k = 1, \ldots, n \tag{4.4}$$

$$U = \left\{ M(\mathbf{v}^1 \cdot \mathbf{p}^k),\ M(\mathbf{v}^2 \cdot \mathbf{p}^k), M(\mathbf{v}^3 \cdot \mathbf{p}^k) \right\}, \quad \forall\ k = 1, \ldots, n \tag{4.5}$$

As the i-th axis of the OBB is aligned with $\mathbf{v}^i$, the OBB's edge half-length h_i along this axis is given by:

$$h_i = \frac{u_i - l_i}{2}, \quad i = 1,2,3 \tag{4.6}$$

and the center point $\mathbf{c}$ of the OBB is given by:

$$\mathbf{c} = \frac{1}{2} \sum_{i=1}^{3} (l_i + u_i) \mathbf{v}^i \tag{4.7}$$

These parameters define also the ellipsoid inscribed into the OBB, whose principal axes have lengths $a = 2h_1$, $b = 2h_2$, and $c = 2h_3$. We prefer to represent the ellipsoid with the full-axes length instead of the semi-axes length in order to be consistent with the equations used to compute the sphericity and roundness indices (see Sec. 2.2).

The covariance matrix can be built from the corresponding voxel model using the voxel coordinates as representative points. The first contribution of this paper is to use the extreme vertices (EV) of the EVM-represented object as the set of representative points. Although the number of EV is significantly smaller than the number of voxels, the OBB produced from the EVM is very similar to the OBB produced from the voxel model. From the analysis of the test

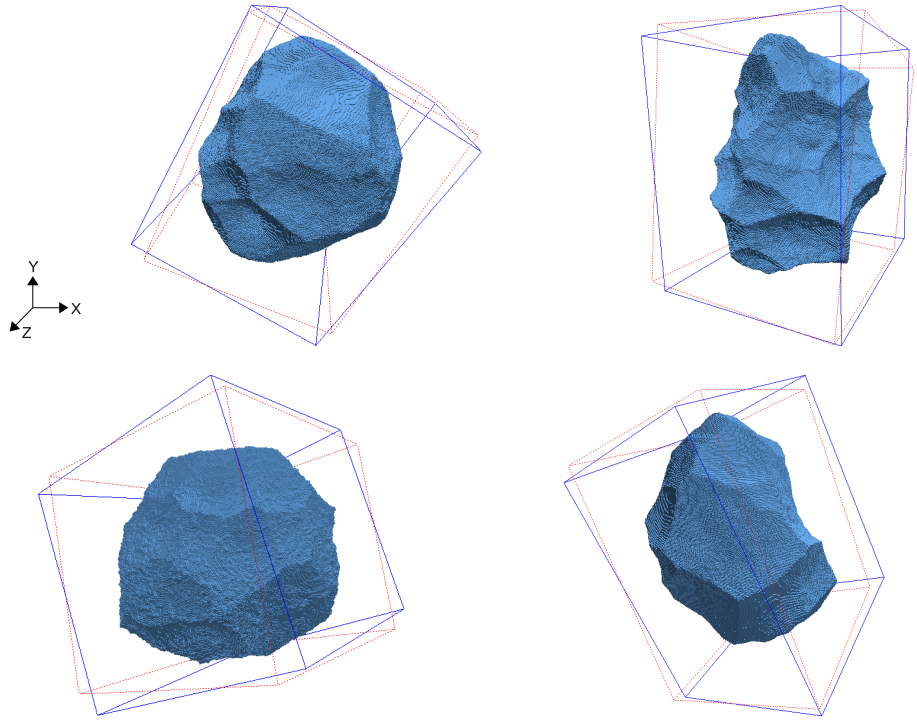

Figure 4.2: Four rock samples and their OBB. The EVM-based and voxel-based OBB in continuous (blue) and stippled (red) line respectively.

samples, the maximum volume difference computed between a voxel-based and a EVM-based OBB was less than 8.5%, while the computation time is greatly reduced in the EVM-based method. Fig. 4.2 shows some samples and their computed OBB.

4.2 Sphericity Computation

Given an input object, the OBB is computed first. Then, the sphericity indices given by Eq. 2.2 to 2.5 can be directly computed from the three principal axes lengths (a, b, c) of the inscribed ellipsoid. To compute the true sphericity index (Eq. 2.1), the surface area of the object is required. Because of the nature of EVM, the surface area of an EVM-represented object is measured with a block-form surface extraction algorithm [31] and therefore, this method is not suitable to estimate the object's continuous surface area. However, there are voxel-based methods that better estimate this value for binary volumes.

The surface area is estimated using a voxel-based scheme [23, 43], which is unbiased for random plane orientations with small error when applied to curved surfaces. The algorithm detects all the surface voxels (voxels with 6-connectivity to background voxels) and classifies them into nine classes (denoted S_1 to S_9) according to the number and configuration of its faces that are exposed to the background (see Fig. 4.3). Then, the surface area $\mathcal{S}$, is estimated as a linear

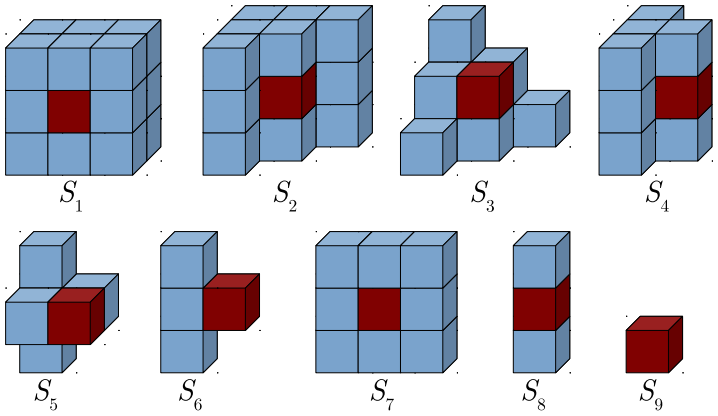

Figure 4.3: The nine unique surface voxel classes (modulo reflections and rotations) [43].

combination of the class membership values N_i.

$$\mathcal{S} = \sum_{i=1}^{9} W_i N_i \tag{4.8}$$

The optimal computed weights W_i associated with the voxels in classes S_i are: $W_1 \approx 0.894$, $W_2 \approx 1.3409$, $W_3 \approx 1.5879$, $W_4 = 2$, $W_5 = \frac{8}{3}$, $W_6 = \frac{10}{3}$ [23], $W_7 \approx 1.79$, $W_8 \approx 2.68$, $W_9 \approx 4.08$ [43].

4.3 Roundness Computation

In industrial engineering, the roundness measurement of workpieces is estimated by doing a single 2D trace covering 360° of the workpiece, this process is usually performed with a turntable-type instrument or a stylus-type instrument [28]. The deviation of the trace from a least-squares circle fit to the data at equally spaced angles θ_i gives a roundness estimation of $d_i - r$, where r is the radius of the circle and d_i the distance from the circle center to the trace [24]. A set of random, uniformly distributed, rays can be traced to the surface of a reference ellipsoid [38].

Based on this previous idea, we propose a new 3D roundness index computation method. The deviations of the rays from the surface of the object gives a roundness estimation. For efficiency purposes, instead of generating a set of uniformly distributed rays, we propose to trace rays to each EV in the EVM-represented object. Then, to compute the proposed EVM-roundness index, three steps are performed:

1. Compute the object's OBB to obtain the principal axes of the ellipsoid inscribed in this OBB (reference ellipsoid).

2. Create a transformation matrix $\mathbf{M}$, which transforms the OBB so that it is aligned to the main coordinate axes and centered at the origin in order to facilitate subsequent computations. Apply this transformation to all the EV of the object.

3. Trace a ray from the origin to each EV representing point $\mathbf{p}^k$ of the object, and measure the distance Δ_k between $\mathbf{p}^k$ and the point $\mathbf{q}^k$, where the ray intersects the surface of the reference ellipsoid.

The first step computes the OBB with the method described in Sec. 4.1 (see Fig. 4.4(a)). The second steps creates a transformation matrix $\mathbf{M}$, which is a composition of a translation matrix and three rotation matrices. Fig. 4.4(b) shows the EV set of an object and the reference ellipsoid after transformation. Note that the OBB bounds both the object and the reference ellipsoid, but the object and the ellipsoid may intersect each other. The third step applies the algorithm for ray-sphere intersection [36] properly adjusted for an ellipsoid (see Fig. 4.4(c)).

The ray has an equation of the form $\mathbf{q} = \mathbf{p}^0 + t\mathbf{p}$. Let $\mathbf{p}^0$ be the origin $(0, 0, 0)$, then, the point $\mathbf{q}^k = (q_1^k, q_2^k, q_3^k)$ where the ray, passing by the EV point $\mathbf{p^k} = (p_1^k, p_2^k, p_3^k)$, crosses the ellipsoid with center at $\mathbf{p}^0$ and principal axes lengths a, b and c, can be computed solving the next quadratic equation for t:

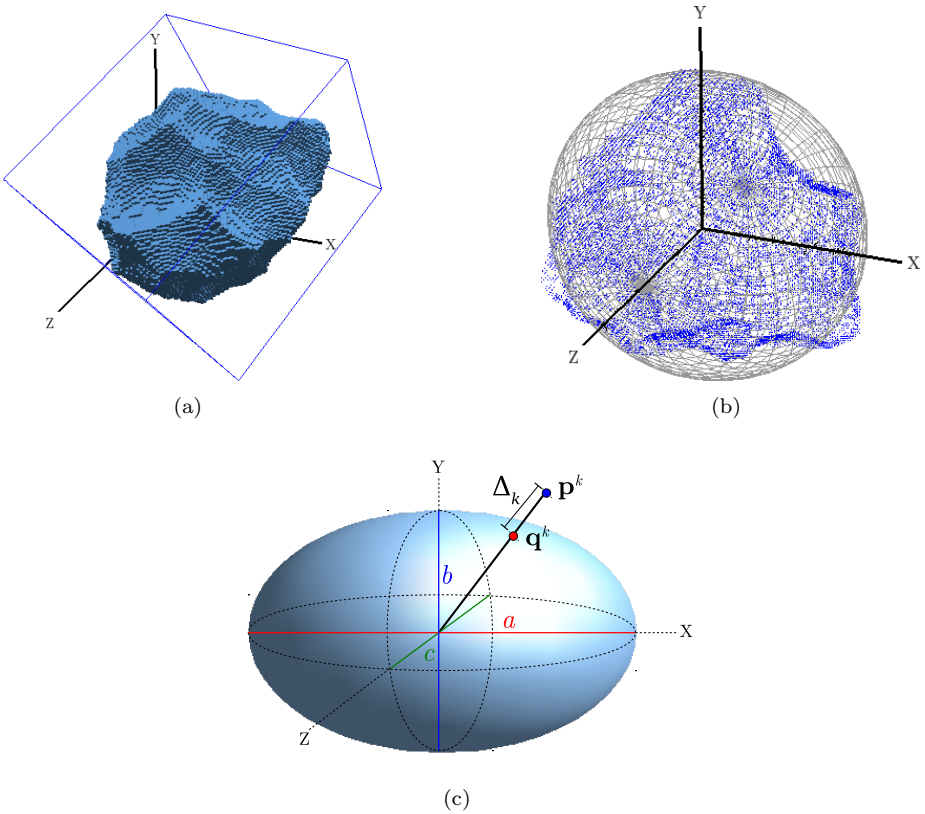

Figure 4.4: Steps to compute the EVM-roundness. (a) Calculate the OBB. (b) Transform the model such that the reference ellipsoid is centered at the origin and aligned to the main coordinate axes. (c) Trace rays to each EV $\mathbf{p}^k$ and compute Δ_k.

$$t^2|\mathbf{p}^{k\prime}|^2 - 1 = 0, \text{ where } \mathbf{p}^{k\prime} = \left(\frac{2p_1^k}{a}, \frac{2p_2^k}{b}, \frac{2p_3^k}{c}\right) \tag{4.9}$$

therefore,

$$\mathbf{q}^k = (tp_1^k, tp_2^k, tp_3^k) \tag{4.10}$$

$$\Delta_k = |\mathbf{p}^k - \mathbf{q}^k| \tag{4.11}$$

We define the EVM-roundness index as the average of the distances Δ_k for all EV representing points $\mathbf{p}^k$. As the measurements depend on the size of the input object, to remove the size effect, the average is divided by a length factor. There are several alternatives for this factor, e.g., the principal axes lengths (a, b, or c), the geometric mean of them or the corresponding arithmetic mean. We have adopted the geometric mean because the EVM-roundness index is compared with a method that uses this length factor. The average is also multiplied by a factor of 10 to enhance the readability of the results.

$$\mathcal{R} = \frac{10}{n(abc)^{\frac{1}{3}}} \sum_{k=1}^{n} \Delta_k \tag{4.12}$$

where n is the number of extreme vertices.

Chapter 5

EVM-roundness Correlation

In order to show the correlation of the EVM-roundness index with the roundness index defined by Wadell, the silhouettes of the Krumbein's chart (Fig. 2.1) have been tested in a 2D version of the proposed method. Each tested image has a resolution of $\approx 320^2$ pixels. Fig. 5.1 shows the relationship between Krumbein's roundness and EVM-roundness. These results have a linear correlation of -0.898 (negative as Krumbein's roundness index decreases while EVM-roundness index increases). The EVM-roundness index has also been computed applying the OBB computed from the voxel model. It results in a better, but not very different correlation of -0.902.

For a comparison in 3D, the roundness index proposed by Hayakawa and Oguchi (HO-roundness) (see Eq. 2.7) has also been computed. To get the HO-roundness, the surface area of the object is measured using the voxel-based

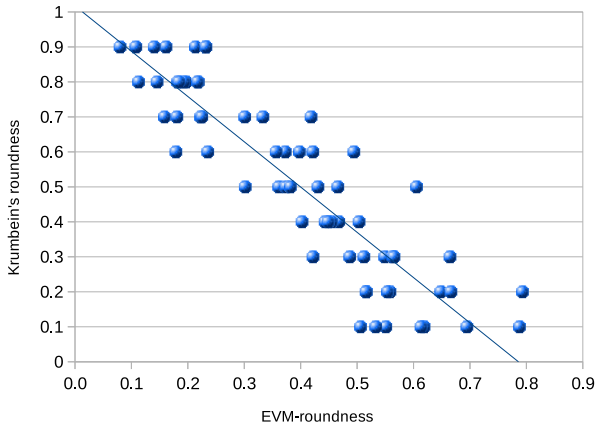

Figure 5.1: Relationship between Krumbein's chart roundness and EVM-roundness.

scheme described in Sec. 4.2.

We have used a GPL Blender extension, *rock Generator* (wiki.blender.org) to create a set of thirty 3D models of rocks (see Fig. 5.2). Each model was converted to a voxel model with a resolution of $\approx 250^3$ voxels. Distribution of the set of rocks according to their computed sphericity and roundness is shown in Fig. 5.3. The relationship between HO-roundness and EVM-roundness indices is shown in Fig. 5.4. In this case, the results have a correlation of -0.938.

The corresponding programs have been written in C++ and tested on a PC Intel®Core 2 Duo CPU E6600@2.40GHz with 3.2 GB RAM and running Linux. In this PC, the time to compute the HO-roundness index for each rock sample is about 2 seconds, while for the EVM-roundness index, it is about 0.1 seconds.

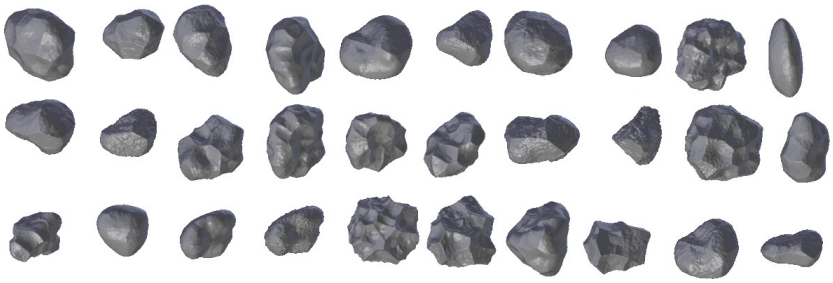

Figure 5.2: Thirty 3D rock samples created with rockGenerator.

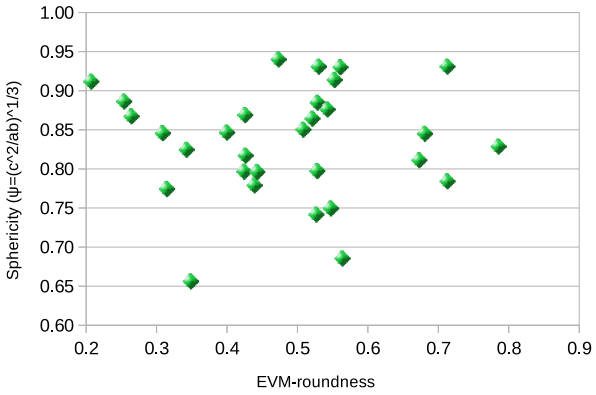

Figure 5.3: Distribution of the rocks samples according to their sphericity and roundness.

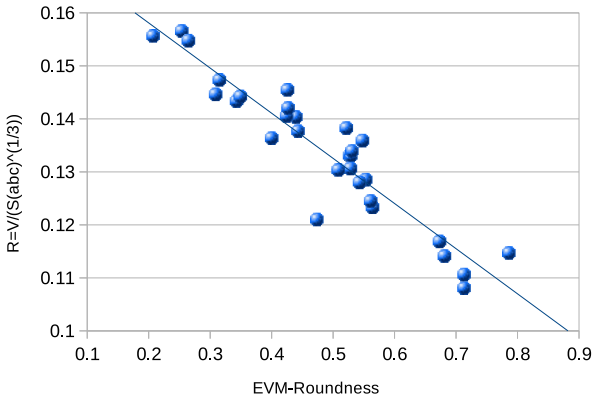

Figure 5.4: Relationship between HO-roundness and EVM-roundness.

Chapter 6

Analysis of Real Silica nano CT

Silica sands need to have a high sphericity, as where the more round and spherical is the particle, the more resistant that particle is to crushing or fragmenting [35]. We have been provided with a silica nano CT by the Laboratory of Electron Nanoscopies of the University of Barcelona. It consists of a 32-bit gray scale dataset in RAW format with dimensions $131 \times 281 \times 332$. Some 2D slices of this dataset are depicted in Fig. 6.1.

In order to obtain the sphericity and roundness indices, the dataset needs to be preprocessed. This preprocessing basically consists of the next steps:

1. Convert the original dataset to a 8-bit voxel model.
2. Scale the voxel model, via trilinear interpolation, to twice its size in order to better define the grain shapes.
3. Apply a binary threshold filter.
4. Remove noise applying morphological opening and closing operations.

Step 3 requires a threshold that allows to yield a good segmentation of the grain shapes. The gray value histogram is shown in Fig. 6.2, in this case, high

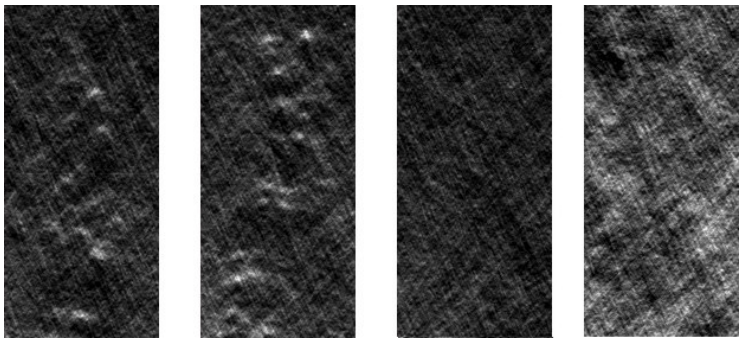

Figure 6.1: 2D slices of a silica nano CT.

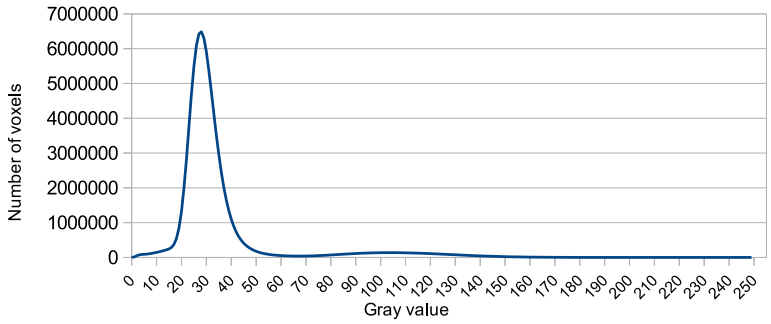

Figure 6.2: Gray value histogram of the sample.

values of gray represent the foreground and the curve helps to determine where the background ends and the foreground begins. Note that the curve falls off around the value of 50. Therefore, thresholds of 45, 50 and 55 have been used to binarize the dataset. Fig. 6.3 shows the sample after the corresponding threshold and noise removal indicating the number of connected components (CC) considering 6-connectivity. Observe that the threshold of 45 produce a model having several agglomerated grains and the threshold of 55 seems to lose information. Then, we consider that the grain shapes are better defined applying a threshold of 50.

After the preprocessing, we compute the CC, which represent the grain particles. Fig. 6.4 shows a graph of the number of CC according to their volumes. CC having a very small volume are not representative of a grain particle, then, according to this graph, we consider as grains those CC with a volume larger than 200 voxels (shapes larger than approximately 6×6×6). Therefore, the resulting dataset consists of 650 CC. See Fig. 6.5 where the resulting grains are depicted.

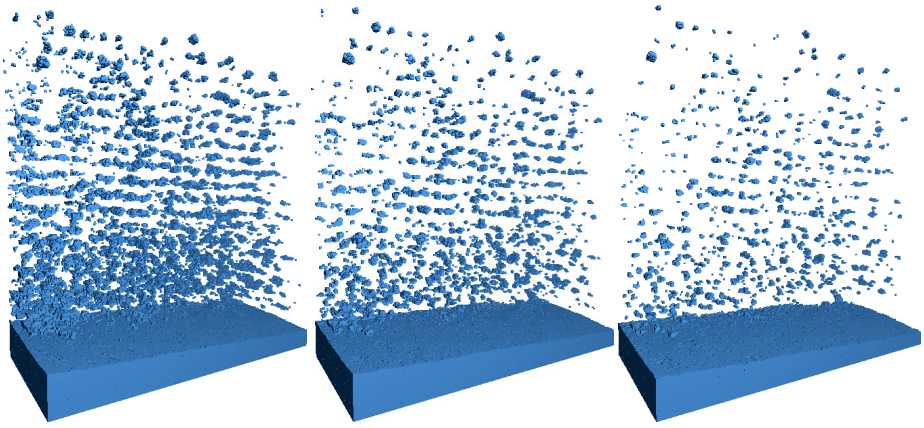

(a) CC=1894 (b) CC=1181 (c) CC=753

Figure 6.3: Dataset after segmentation and noise removal with thresholds (a) 45, (b) 50 and (c) 55.

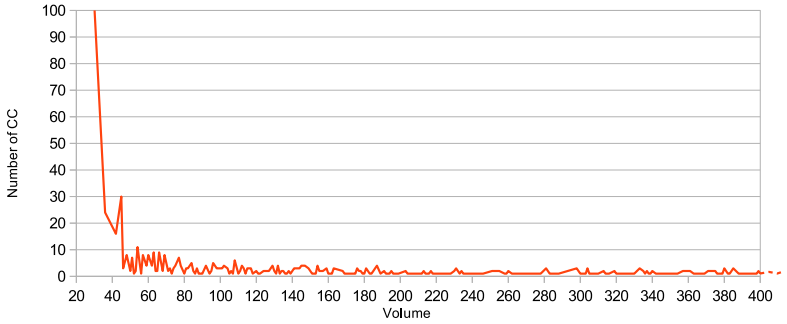

Figure 6.4: Number of connected components according to their volumes.

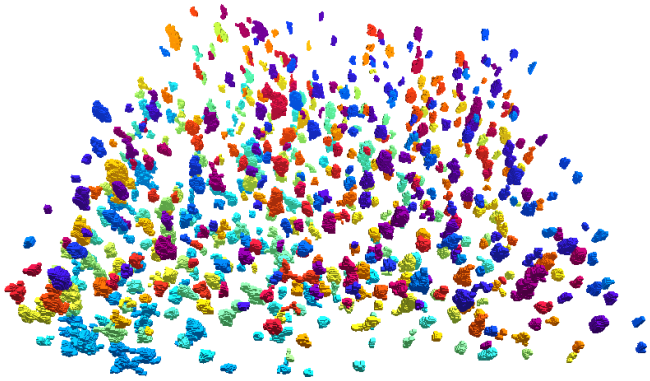

Figure 6.5: Resulting grain particles with volume larger than 200 voxels.

6.1 Grain Properties Computation

After the grain particles have been correctly defined, they are converted to its EVM-representation in order to compute its sphericity and roundness indices.

The sphericity index of each connected component is computed using Eq. 2.1 and 2.5. Fig. 6.6 and 6.7 show the bar charts that represent the number of occurrences of the corresponding sphericity index. Although the voxel-based scheme used to compute the surface area (see Sec. 4.2) is not well suited for too small objects, both graphs are similar and give an estimation of the sphericity distribution.

Regarding roundness, for each connected component, its 3D roundness index is computed using Eq. 2.7 and the presented EVM-based roundness method (see Sec. 4.3). Fig. 6.8 and 6.9 show the bar charts that represent the number of occurrences of the corresponding roundness indices. Again, although the roundness indices are computed using different approaches, both graphs are similar and give an estimation of the roundness distribution.

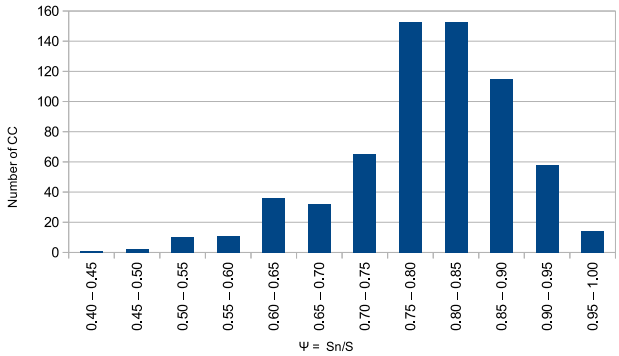

Figure 6.6: Occurrences of sphericity indices using Eq. 2.1.

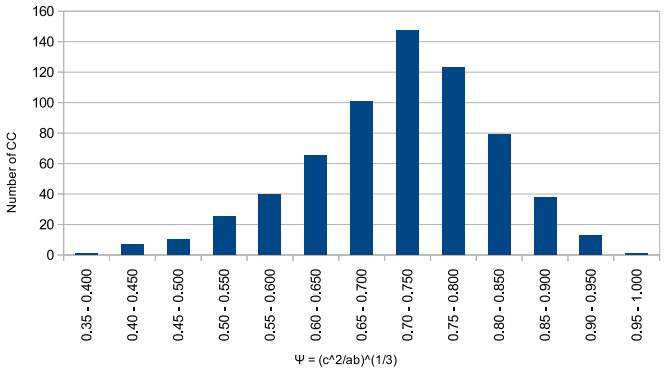

Figure 6.7: Occurrences of sphericity indices using Eq. 2.5.

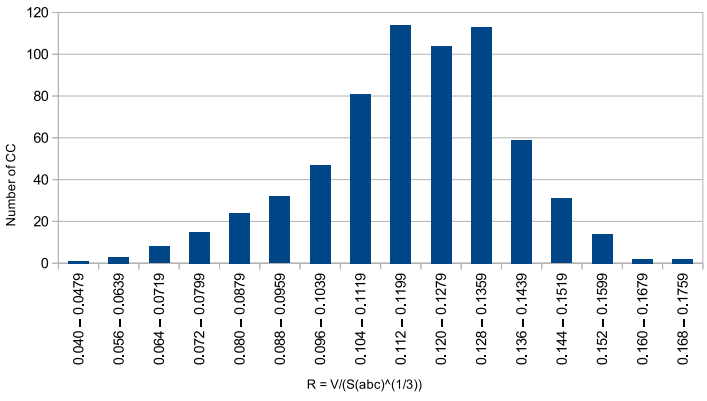

Figure 6.8: Occurrences of roundness indices using Equation 2.7.

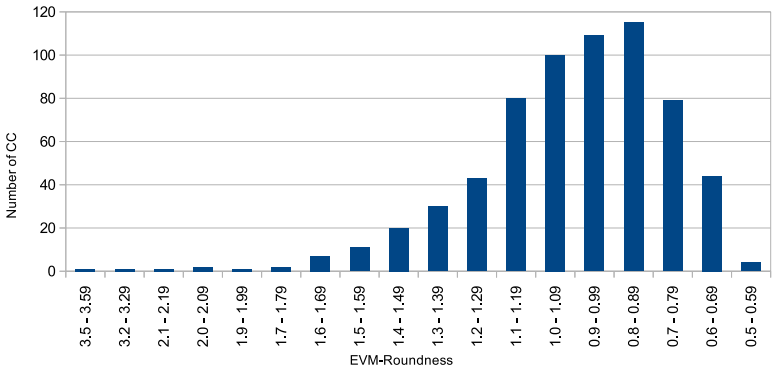

Figure 6.9: Occurrences of roundness indices using Equation 4.12 (EVM-roundness).

Chapter 7

Conclusions

We have presented alternative methods to compute the orientation, sphericity and roundness of particles represented as binary volume datasets.

The method to estimate the sphericity is based on the computation of the object's OBB, which can be computed in a faster way directly from EVM. From the three OBB edge lengths, several sphericity indices can be computed, including the true sphericity index where a voxel-based scheme is applied to estimate the real surface area of curved surfaces.

Regarding the roundness, we have proposed a new EVM-based roundness index. The method is based on the trace of rays to the vertices of the EVM-represented object and their intersections with a reference ellipsoid. The resulting roundness index shows a good correlation with the Krumbein's chart and a better correlation with a previous 3D roundness index. Besides, the time to compute the proposed index is very fast compared with previous voxel-based and manual methods.

Moreover, results of the analysis of the silica nano CT presented here have been used by experts in nanotechnology who are interested in segmenting and analyzing the sphericity and roundness of this sample.

Bibliography

[1] A. Aguilera. *Orthogonal Polyhedra: Study and Application.* PhD thesis, LSI-Universitat Politècnica de Catalunya, 1998.

[2] A. Aguilera and D. Ayala. Orthogonal Polyhedra as Geometric Bounds in Constructive Solid Geometry. In *Fourth ACM Symposium on Solid Modeling and Applications*, pages 56 – 67. ACM, 1997.

[3] T. Biedl and B. Genç. Reconstructing orthogonal polyhedra from putative vertex sets. *Computational Geometry*, 44(8):409 – 417, 2011.

[4] A. Biswas, P. Bhowmick, M. Sarkar, and B. B. Bhattacharya. A linear-time combinatorial algorithm to find the orthogonal hull of an object on the digital plane. *Information Sciences*, 216(0):176 – 195, 2012.

[5] O. Bournez, O. Maler, and A. Pnueli. Orthogonal polyhedra: Representation and computation. *Hybrid Systems: Computation and Control*, pages 46–60, 1999. LNCS 1569, Springer.

[6] A. T. Corey. *Influence of shape on the fall velocity of sand grains.* Audio Visual Service, Colorado State University., 1963.

[7] I. Cruz-Matías and D. Ayala. An efficient alternative to compute the genus of binary volume models. In *Proc. of the Int. Conf. GRAPP 2013*, pages 18–26. SciTePress, 2013.

[8] I. Cruz-Matías and D. Ayala. Merging faces: A new orthogonal simplification of solid models. In *DGCI*, volume 7749 of *Lecture Notes in Computer Science*, pages 143–154. Springer-Verlag, 2013.

[9] M. Diepenbroek, A. Bartholomä, and H. Ibbeken. How round is round? a new approach to the topic 'roundness' by fourier grain shape analysis. *Sedimentology*, 39(3):411–422, 1992.

[10] G. Drevin and L. Vincent. Granulometric determination of sedimentary rock particle roundness. In *Proceedings of International Symposium on Mathematical Morphology (ISMM)*, pages 315–325, 2002.

[11] D. Eppstein and E. Mumford. Steinitz theorems for orthogonal polyhedra. In *Proceedings of the 2010 annual symposium on Computational geometry*, pages 429–438. ACM, 2010.

[12] C. Esperança and H. Samet. Vertex representations and their applications in computer graphics. *The Visual Computer*, 14:240–256, 1998.

[13] S. Gottschalk. *Collision queries using oriented bounding boxes*. PhD thesis, The University of North Carolina, 2000.

[14] S. Gottschalk, M. C. Lin, and D. Manocha. OBBTree: a hierarchical structure for rapid interference detection. In *Proceedings of SIGGRAPH '96*, pages 171–180. ACM, 1996.

[15] D. J. Graham and N. G. Midgley. Graphical representation of particle shape using triangular diagrams: an excel spreadsheet method. *Earth Surface Processes and Landforms*, 25(13):1473–1477, 2000.

[16] K. D. M. Harris, M. Tremayne, and B. M. Kariuki. Contemporary advances in the use of powder X-ray diffraction for structure determination. *Angewandte Chemie International Edition*, 40(9):1626–1651, 2001.

[17] Y. Hayakawa and T. Oguchi. Evaluation of gravel sphericity and roundness based on surface-area measurement with a laser scanner. *Computers & geosciences*, 31(6):735–741, 2005.

[18] M. Khachan, P. Chenin, and H. Deddi. Polyhedral representation and adjacency graph in n-dimensional digital images. *Computer Vision and Image understanding*, 79:428 – 441, 2000.

[19] J. H. Kinney, J. S. Stolken, T. S. Smith, J. T. Ryaby, and N. E. Lane. An orientation distribution function for trabecular bone. *Bone*, 36:193 – 201, 2005.

[20] W. C. Krumbein. Measurement and geological significance of shape and roundness of sedimentary particles. *Journal of Sedimentary Research*, 11(2):64–72, 1941.

[21] J. Lachaud and A. Montanvert. Continuous analogs of digital boundaries: A topological approach to iso-surfaces. *Graphical Models*, 62:129 – 164, 2000.

[22] J. Martínez, N. Pla, and M. Vigo. Skeletal representations of orthogonal shapes. *Graphical Models*, 75:189 – 207, 2013.

[23] J. C. Mullikin and P. W. Verbeek. Surface area estimation of digitized planes. *Bioimaging*, 1(1):6–16, 1993.

[24] M. Natrella. *NIST/SEMATECH e-Handbook of Statistical Methods*. NIST/SEMATECH, July 2010.

[25] T. P. Nguyen and I. Debled-Rennesson. Curvature estimation in noisy curves. In *Computer Analysis of Images and Patterns*, pages 474–481. Springer, 2007.

[26] A. Odgaard. Three-dimensional methods for quantification of cancellous bone architecture. *Bone*, 20(4):315 – 328, 1997.

[27] S. C. Park and B. K. Choi. Boundary extraction algorithm for cutting area detection. *Computer-Aided Design*, 33(8):571–579, 2001.

[28] L. Rico, A. Naranjo, S. Noriega, E. Martínez, and L. Vidal. Effect of cutting parameters on the roundness of cylindrical bars turned of 1018 steel. *Measurements*, 2010.

[29] J. Rodríguez, D. Ayala, and A. Aguilera. *Geometric Modeling for Scientific Visualization*, chapter EVM: A Complete Solid Model for Surface Rendering, pages 259–274. Springer-Verlag, 2004.

[30] J. Rodríguez, I. Cruz, E. Vergés, and D. Ayala. A connected-component-labeling-based approach to virtual porosimetry. *Graphical Models*, 73:296–310, 2011.

[31] J. E. Rodríguez. *Contribution to Surface/Volume Integration: A Model for Visualization and Manipulation.* PhD thesis, LSI-UPC, 2004.

[32] T. Roussillon, H. Piégay, I. Sivignon, L. Tougne, and F. Lavigne. Automatic computation of pebble roundness using digital imagery and discrete geometry. *Computers & Geosciences*, 35(10):1992–2000, 2009.

[33] K. I. Rybakov, V. Semenov, G. Link, and M. Thumm. Preferred orientation of pores in ceramics under heating by a linearly polarized microwave field. *Journal of Applied Physics*, 101(8):084915–084915–5, 2007.

[34] N. Sahu and S. Panigrahi. Mathematical aspects of rietveld refinement and crystal structure studies on pbtio3 ceramics. *Bulletin of Materials Science*, 34(7):1495–1500, 2011.

[35] M. Schroth, J. Istok, S. Ahearn, and J. Selker. Characterization of miller-similar silica sands for laboratory hydrologic studies. *Soil Science Society of America Journal*, 60(5):1331–1339, 1996.

[36] P. Shirley, M. Ashikhmin, M. Gleicher, S. Marschner, E. Reinhard, K. Sung, W. Thompson, and P. Willemsen. *Fundamentals of computer graphics.* AK Peters Natick, 2002.

[37] E. D. Sneed and R. L. Folk. Pebbles in the lower colorado river, texas a study in particle morphogenesis. *The Journal of Geology*, pages 114–150, 1958.

[38] Y. Tashiro. On methods for generating uniform random points on the surface of a sphere. *Annals of the Institute of Statistical Mathematics*, 29(1):295–300, 1977.

[39] E. Vergés, D. Tost, D. Ayala, E. Ramos, and S. Grau. 3D pore analysis of sedimentary rocks. *Sedimentary Geology*, 234(1–4):109–115, 2011.

[40] M. Vigo, N. Pla, D. Ayala, and J. Martínez. Efficient algorithms for boundary extraction of 2D and 3D orthogonal pseudomanifolds. *Graphical Models*, 74:61–74, 2012.

[41] H. Wadell. Volume, shape, and roundness of rock particles. *The Journal of Geology*, 40:443–451, 1932.

[42] H. Wadell. Sphericity and roundness of rock particles. *The Journal of Geology*, 41(3):310–331, 1933.

[43] G. Windreich, N. Kiryati, and G. Lohmann. Voxel-based surface area estimation: from theory to practice. *Pattern Recognition*, 36(11):2531–2541, 2003.